Correlations Among Near-Infrared and Short-Wavelength Autofluorescence and Spectral-Domain Optical Coherence Tomography in Recessive Stargardt Disease

Tobias Duncker,[1,2] Marcela Marsiglia,[1] Winston Lee,[1] Jana Zernant,[1] Stephen H. Tsang,[1,3] Rando Allikmets,[1,3] Vivienne C. Greenstein,[1] and Janet R. Sparrow[1,3]

[1]Department of Ophthalmology, Columbia University, New York, New York, United States
[2]Department of Ophthalmology, Charité, University Medicine Berlin, Berlin, Germany
[3]Department of Pathology and Cell Biology, Columbia University, New York, New York, United States

Correspondence: Janet R. Sparrow, Department of Ophthalmology, Columbia University, 630 West 168th Street, New York, NY 10032, USA; jrs88@columbia.edu.

Submitted: May 21, 2014
Accepted: October 14, 2014

Citation: Duncker T, Marsiglia M, Lee W, et al. Correlations among near-infrared and short wavelength autofluorescence and spectral-domain optical coherence tomography in recessive Stargardt disease. *Invest Ophthalmol Vis Sci*. 2014;55:8134–8143. DOI:10.1167/iovs.14-14848

Purpose. Short-wavelength (SW) fundus autofluorescence (AF) is considered to originate from lipofuscin in retinal pigment epithelium (RPE) and near-infrared (NIR) AF from melanin. In patients with recessive Stargardt disease (STGD1), we correlated SW-AF and NIR-AF with structural information obtained by spectral-domain optical coherence tomography (SD-OCT).

Methods. Twenty-four STGD1 patients (45 eyes; age 8 to 61 years) carrying confirmed disease-associated *ABCA4* mutations were studied prospectively. Short-wavelength AF, NIR-AF, and SD-OCT images were acquired.

Results. Five phenotypes were identified according to features of the central lesion and extent of fundus change. Central zones of reduced NIR-AF were typically larger than areas of diminished SW-AF and reduced NIR-AF usually approximated areas of ellipsoid zone (EZ) loss identified by SD-OCT (group 1; r, 0.93, $P < 0.0001$). In patients having a central lesion with overlapping parafoveal rings of increased NIR-AF and SW-AF (group 3), the extent of EZ loss was strongly correlated with the inner diameter of the NIR-AF ring (r, 0.89, $P < 0.0001$) and the eccentricity of the outer border of the NIR-AF ring was greater than that of the SW-AF ring.

Conclusions. Lesion areas were more completely delineated in NIR-AF images than with SW-AF. In most cases, EZ loss was observed only at locations where NIR-AF was reduced or absent, indicating that RPE cell atrophy occurs in advance of photoreceptor cell degeneration. Because SW-AF was often increased within the central area of EZ disruption, degenerating photoreceptor cells may produce lipofuscin at accelerated levels. Consideration is given to mechanisms underlying hyper–NIR-AF in conjunction with increased SW-AF.

Keywords: ABCA4, fundus autofluorescence, lipofuscin, melanin, optical coherence tomography, recessive Stargardt disease, retinal pigment epithelium, scanning laser ophthalmoscope

Fundus imaging has been central to the clinical diagnosis and monitoring of patients with recessive Stargardt disease (STGD1). For instance, fluorescein angiography can be used to identify STGD1 patients, the masking of choroidal fluorescence by RPE lipofuscin (dark choroid) being considered a sign of STGD1,[1] in most cases.[2] Noninvasive imaging by confocal laser scanning ophthalmoscopy has revealed that patients with STGD1 present with abnormalities in fundus autofluorescence (AF) patterns; these abnormalities include spatial heterogeneities that confer AF texture,[3,4] AF intensity loss,[5] and hyper-autofluorescent foci (flecks).[6,7] STGD1 also is associated with elevated intensities of fundus AF[4,8] due to an exaggerated build-up of the vitamin A-aldehyde-adducts that constitute the lipofuscin of RPE cells.[9,10] The accelerated formation of these lipofuscin fluorophores occurs in photoreceptor cells due to mutations in the gene encoding the ATP-binding cassette (ABC) transporter ABCA4.[11–14] And finally, with imaging by optical coherence tomography (OCT), changes in the reflectivity bands have disclosed photoreceptor cell loss[15] with RPE/Bruch's membrane thinning and pronounced sub-RPE hyperreflectivity being indicative of RPE atrophy.[10,16]

Besides short-wavelength (SW) excitation, fundus AF can be elicited by near-infrared (NIR) excitation. Although fundus AF generated by SW exciting light originates predominantly from RPE lipofuscin,[17] NIR-AF is emitted from melanin in both RPE and choroid, with the contribution from the choroid varying according to the race and iris color of an individual.[18]

Despite the utility of SW- and NIR-AF imaging in STGD1 disease, some observations have been perplexing. For instance, although both modalities are thought to originate from RPE, discrepancies can occur as to the boundaries of geographic atrophy (GA). Specifically, zones of RPE atrophy appear larger in NIR-AF images than in SW-AF images.[16,19] Additionally, in areas of atrophy, the ellipsoid zone (EZ) in spectral-domain (SD) OCT images can be absent at fundus locations wherein the RPE appears to be intact based on the presence of a SW-AF signal.[20,21] These incongruities are important, as the interpretations speak to the issue of whether photoreceptor cell degeneration precedes or follows RPE loss in STGD1 disease.

Imaging by SW-AF and NIR-AF in tandem can provide complementary information. To better appreciate the clinical significance of AF patterns and to understand the origins of NIR-AF and SW-AF in the presence of retinal disease, we sought to establish correlations with underlying retinal structure. In this multimodal study, we have therefore compared changes in NIR-AF and SW-AF with structural features visible in SD-OCT images. In the latter case, particular attention was given to the integrity of the EZ.

Methods

Subjects

The study cohort consisted of 24 prospectively recruited patients (45 eyes; 22 families; 10 patients were female) with early to intermediate disease stages. For the purpose of this study, patients with advanced disease (loss of the NIR-AF signal throughout the 30° field, complete EZ disruption throughout the 9-mm SD-OCT scan) were excluded. The mean age of the patients was 26.5 years (range, 8 to 61 years). Clinical, demographic, and genetic data for all patients are presented in Table 1. At least one known mutation in the *ABCA4* gene was detected in all patients and two mutations were detected in 16 (67%) of 24 patients. Patients had a complete eye examination and the clinical diagnosis of STGD1 was confirmed by a retinal specialist. All procedures adhered to the tenets of the Declaration of Helsinki, and written informed consent was obtained from all subjects after a full explanation of the procedures was provided. The protocol was approved by the Institutional Review Board of Columbia University.

Genotyping

The ABCR600 microarray (Asper Biotech, Inc., Tartu, Estonia; www.asperbio.com), which detects the 632 currently known mutations in the *ABCA4* gene, was used for initial screening in most patients. Detected variants were confirmed by direct Sanger sequencing. More recently when *ABCA4* mutations were not detected by the microarray, next-generation sequencing of the entire *ABCA4* open reading frame and adjacent intronic sequences was performed on the Roche 454 platform.[22]

Imaging

Pupils were dilated with topical 1% tropicamide and 2.5% phenylephrine. Short-wavelength AF images (30°, 488-nm excitation) were acquired with the Spectralis HRA+OCT (Heidelberg Engineering, Heidelberg, Germany) after bleaching of photopigments for 20 seconds in AF mode.[23] In addition, a horizontal 9-mm SD-OCT image through the fovea was recorded with the Spectralis and automatically registered to a simultaneously acquired near-infrared reflectance (NIR-R) fundus image. Near-infrared AF images (30°, 787-nm excitation) were acquired with the HRA2 (Heidelberg Engineering) using the indocyanine-green angiography mode (without dye injection). Even though the intensity of NIR-AF is considerably less than the intensity of SW-AF, through the eye-tracking function of the HRA2 and averaging of up to 100 single frames, high-quality NIR-AF images were obtained. Color images were acquired with a FF450+IR fundus camera (Carl Zeiss Meditech, Jena, Germany). All images of the same field were aligned to the NIR-R image of the SD-OCT scan using i2kRetina software (DualAlign LLC, Clifton Park, NY, USA). This process allowed us to subsequently correlate NIR-AF, SW-AF, and SD-OCT in the axis of the SD-OCT scan. To illustrate the overlap of AF rings in SW- and NIR-AF images, inner and outer ring borders were outlined in Adobe Photoshop CS5 (Adobe Systems, Inc., San Jose, CA, USA) using the lasso tool. The interior of the rings were then shaded in red (NIR-AF) and blue (SW-AF), and the images were merged.

Two independent operators (MM, WL) analyzed scaled images from patients in groups 1, 3, and 4 (defined below) using the ruler tool in Photoshop CS5 (Adobe, San Jose, CA). In SD-OCT images, distances were measured from the nasal to temporal limits of continuous EZ loss in a transverse plane through the fovea. For group 1, the diameter of the central area of reduced SW-AF and NIR-AF was measured. In SW-AF images of groups 3 and 4, the diameter of the hyperautofluorescent ring was measured in relation to both the inner and outer border of the ring. In NIR-AF images of group 3 the diameter of the hyperautofluorescent ring (in relation to both inner and outer borders) was measured. In NIR-AF images of group 4, the diameter of the low NIR-AF lesion was measured in a plane through central fovea (note that in group 4, NIR-AF rings were not present). Measurements were obtained as pixel values and were then converted to millimeters. Intraclass correlation coefficients (ICCs) were computed to estimate interoperator reliability. Measurements of the two operators were then averaged. Pearson correlation coefficient r was calculated to assess the relationship between EZ loss and the parameters measured in the SW-AF and NIR-AF images. Groups 2 and 5 were not amenable to quantitative analysis. In group 2, fundus changes were already too extensive, whereas in group 5, fundus changes were often very localized and subtle.

Results

In a healthy subject (Fig. 1) the distribution of the NIR-AF and SW-AF signal follows a characteristic pattern. Centrally, the NIR-AF signal is high due to increased optical density of melanin in an area approximately 8° in diameter.[18,24] Conversely, the SW-AF signal of the central macula and especially the fovea is reduced due to absorption of the excitation light by photopigment. Outside the central macula, the NIR-AF and SW-AF signals are both relatively uniform, although large choroidal vessels can be visible on NIR-AF in some subjects.[18,25] In SD-OCT images, the outer nuclear layer (ONL) corresponds to a hyporeflective layer and external limiting membrane (ELM), EZ, interdigitation zone (IZ), and RPE/Bruch's membrane (RPE/BM) are represented by four hyperreflective bands, as indicated in Figure 1 (assignment of SD-OCT layers is based on published nomenclature).[26]

In STGD1, fundus changes often first manifest in the central macula and later progress toward the periphery. Accordingly, some STGD1 patients in this study had fundus changes that were confined to central macula, whereas others presented with more widespread disease. To account for these differences, we grouped patients based on phenotypic features expressed in the NIR-AF and SW-AF images: group 1, central lesion with jagged border; group 2, lesion with extensive fundus changes; group 3, central lesion with smooth border and hyperautofluorescent SW-AF and NIR-AF ring; group 4, central lesion with smooth border and no hyperautofluorescent NIR-AF ring; group 5, discrete central lesions better visualized in NIR-AF images. Due to the high symmetry of fundus changes in STGD1, fellow eyes were always assigned to the same group. Images from all eyes included in the study were used to define the groups, whereas only representative images are presented in the figures.

In Figure 2, images from patients 17 and 1 are presented as examples of group 1 (5/24 patients; Table 1). Patients exhibited a central lesion with generalized mottling and jagged

Table 1. Summary of Demographic, Clinical, and Genetic Data

					BCVA, logMAR		*ABCA4* Mutation		
Patient No.	**Age**	**Sex**	**Ethnicity**	**Iris Color**	**OD**	**OS**	**Allele 1**	**Allele 2**	**Patient Group**
1	35.5	F	White	Brown	0.8	0.8	p.G1961E	c.2382+1G>A	1
2	11.4	M	White	Hazel	0.5	0.6	p.[L541P;A1038V]		4
3	8.2	M	White	Hazel	(0.9)	0.9	p.[L541P;A1038V]		4
4	17.9	M	Indian	Brown	0.7	0.9	p.G1961E	c.6729+4_+18del	3
5	12.1	M	White	Green	0.8	0.7	p.G1961E	p.P1380L	3
6	46.4	M	Black	Brown	0.3	0.8	p.T1526M		2
7	42.6	F	White	Brown	1.3	1.3	p.G1961E	p.[L541P;A1038V]	2
8	42.8	M	White	Blue	0.9	0.4	c.571-1G>T		1
9	24.6	F	White	Hazel	0.3	0.2	p.G1961E	p.N96D	5
10	21.9	F	White	Brown	0.3	0.4	p.G1961E	p.N96D	5
11	25.3	M	White	Brown	0.0	0.3	p.G1961E	p.Q1003*	3
12	8.5	M	White	Green	n/a	(n/a)	p.[L541P;A1038V]	p.L2027F	4
13	19.7	M	White	Brown	0.9	0.9	p.G1961E	p.[L541P;A1038V]	5
14	22.4	F	White	Brown	0.8	0.8	p.R212C		3
15	20.2	M	White	Brown	0.9	0.9	p.G1961E	p.P1380L	1
16	27.6	M	Arabic	Brown	0.0	0.0	p.R1300*	p.R2106C	3
17	26.8	M	White	Blue	0.5	0.5	p.G1961E	c.3050+5G>A	1
18	24.9	F	White	Hazel	0.9	0.9	p.G1961E	p.C2150R	5
19	13.2	M	White	Blue	0.9	1.0	p.W821R	p.C2150Y	3
20	61.0	F	White	Green	2.0	0.0	c.250_251insCAAA		2
21	36.3	F	White	Blue	1.3	0.1	p.N1799D		1
22	14.1	F	White	Green	1.0	0.9	p.R1108C	p.Q1412*	2
23	18.6	M	White	Brown	0.9	0.9	p.G1961E	p.A1773V	3
24	53.3	F	White	Blue	0.3	(0.2)	p.R2077W		2

BCVA values in parenthesis indicate fellow eyes that were not included in the study. BCVA, best-corrected visual acuity.

borders on NIR-AF and SW-AF. The central area of EZ loss (indicated by vertical dashed lines) identified on the SD-OCT scan corresponded to reduced NIR-AF signal at positions traversed by the SD-OCT scan line. Within the area of EZ loss, the SW-AF signal also exhibited altered levels of intensity but the area of low SW-AF was smaller than the area of low NIR-AF, leaving the impression of a larger lesion on NIR-AF.

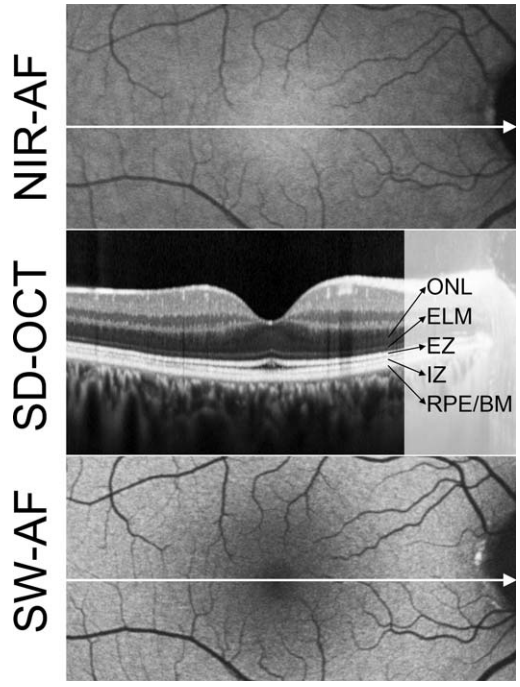

Figure 1. Near-infrared AF, SW-AF, and SD-OCT images of a healthy eye. Outer nuclear layer, ELM, EZ, IZ, RPE/BM. Assignment of retinal layers in the SD-OCT is based on published nomenclature.[26]

Images from patients 24 and 7 (Fig. 3) are representative of group 2 (5/24 patients; Table 1), the latter being characterized by lesions with more extensive fundus changes. The central area of EZ loss (indicated by vertical dashed lines) was located within regions of low NIR-AF. However, low NIR-AF also was observed at eccentricities where EZ was visible yet interrupted. While the low NIR-AF areas appeared confluent, areas of abnormal and normal SW-AF were difficult to distinguish unless the signal was very bright (flecks) or very dark (atrophy). Abnormal SW-AF appeared to overlap with areas of low NIR-AF, but the latter area was larger and easier to delineate.

Images from patients 4, 23, 16, and 14 are presented in Figure 4 as examples of group 3 (7/24 patients; Table 1). All patients had central lesions that were relatively round and had smooth borders on NIR-AF and SW-AF (bull's-eye lesions). In these patients, a central area of low and mottled AF was surrounded by a high AF ring in both modalities. The central area of EZ loss (indicated by vertical dashed lines) correlated with these areas of altered NIR and SW signal. However, in patient 14, an area of low NIR-AF mottling extended beyond the area of EZ loss. In 6 of 7 patients, the high AF rings were homogeneous. In patient 16, the high NIR-AF ring was interrupted by foci of reduced NIR-AF signal and the SW-AF ring contained some bright flecks nasally. The foveal sparing observed in the SD-OCT image of patients 11 and 16 was visible in the NIR-AF image as a circular area that did not have a reduced NIR-AF signal. Conversely, the dark signal on SW-AF due to the presence of macular pigment could be misinterpreted as atrophy.

In Figure 5, the spatial correspondence of the high NIR-AF and SW-AF rings (group 3) are shown for patients 4 and 23 (Table 1; Fig. 4). The NIR-AF (red) and SW-AF (blue) rings overlapped (superimposition of red and blue produces

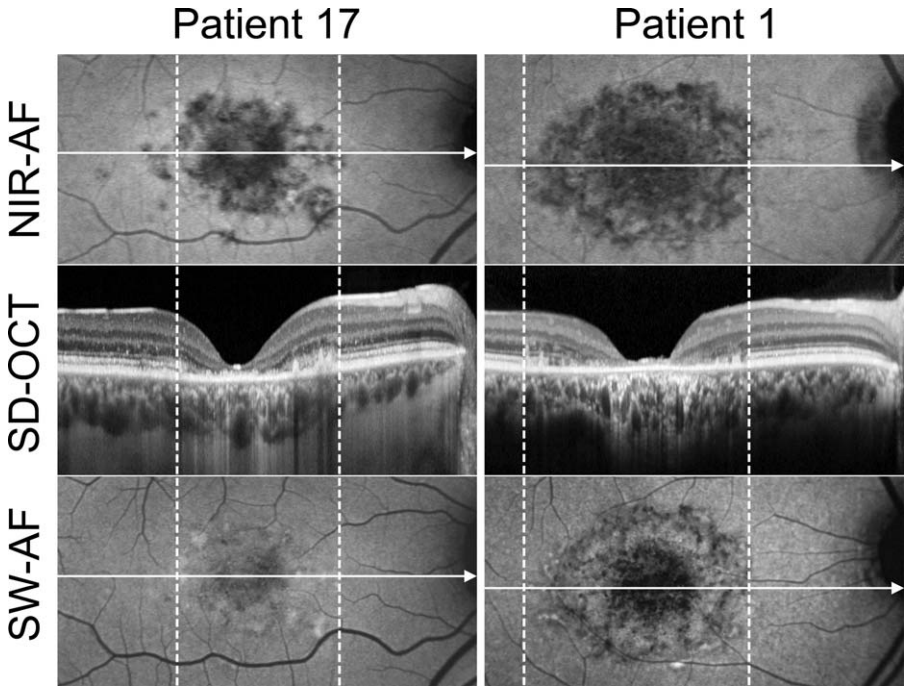

FIGURE 2. Central lesion with jagged border (group 1). Near-infrared AF, SW-AF, and SD-OCT images of patients 17 and 1. Horizontal axis and extent of SD-OCT scan indicated by *arrow* in corresponding NIR-AF and SW-AF images. Area of central EZ loss indicated by *dashed lines*.

magenta) but the NIR-AF ring extended slightly more peripherally. This was also the case for the remaining patients with a round central lesion and a homogeneous high AF ring on both NIR-AF and SW-AF (six patients). The NIR-AF ring extended more peripherally into locations where the EZ was still partially intact.

In Figure 6, images of patients 12, 3, and 2 (group 4, 3/24 patients; Table 1) are presented. These patients also had a central lesion with a round and smooth border but showed features that were different from the patients presented in Figure 4. The central area of EZ loss (indicated by dashed lines) extended further peripherally than the area of low NIR-AF. The EZ gradually thinned toward the lesion and the ELM appeared pronounced. Patients 2 and 3 had a hyperautofluorescent SW-AF ring but a high NIR-AF ring was not visible. The area of low NIR-AF appeared to correlate with the central area of ELM loss.

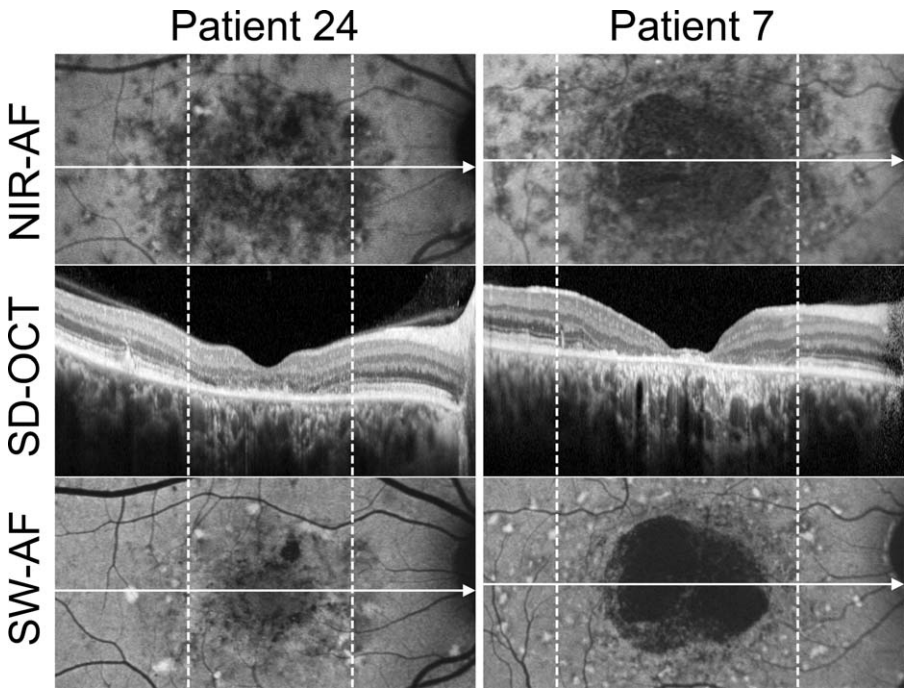

FIGURE 3. Lesions with extensive fundus changes (group 2). Near-infrared AF, SW-AF, and SD-OCT images of patients 24 and 7. Horizontal axis and extent of SD-OCT scan indicated by *arrow* in corresponding NIR-AF and SW-AF images. Area of central EZ loss indicated by *dashed lines*.

Investigative Ophthalmology & Visual Science

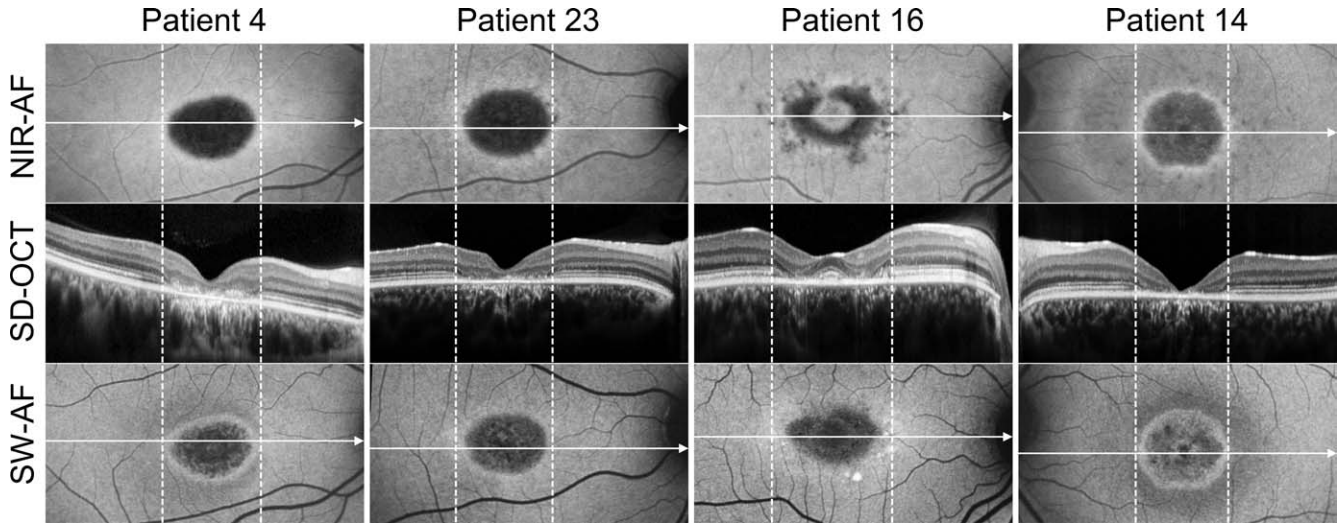

Figure 4. Central lesion with smooth border and hyperautofluorescent SW-AF and NIR-AF ring (group 3). Near-infrared AF, SW-AF, and SD-OCT images of patients 4, 23, 16, and 14. Horizontal axis and extent of SD-OCT scan indicated by *arrow* in corresponding NIR-AF and SW-AF images. Area of central EZ loss indicated by *dashed lines*.

In patient 12, the EZ loss was accompanied by decreased but not absent NIR-AF. In this patient, thinning of the SD-OCT reflective band attributable to RPE/BM was not obvious and the amount of choroidal hyperreflectivity, indicative of RPE atrophy, also was not pronounced. In patients 2 and 3, the NIR-AF signal within the lesion was noticeably lower and there was more choroidal hyperreflectivity accompanied by clearly visible RPE/BM thinning.

Patients 13 and 9 in Figure 7 (group 5, 4/24 patients; Table 1) had a central area of EZ disruption (indicated by vertical dashed lines). The NIR-AF signal was bright centrally; the intensity of this brightness was similar to that in healthy eyes. However, the distribution of the high NIR-AF signal was abnormal. Corresponding changes in the SW-AF signal were difficult to discern due to the presence of macular pigment in this area. Interestingly, patient 13 had an area of low and mottled NIR-AF in a circular area outside the area of EZ loss. In both patients, SD-OCT abnormalities extended beyond the area of EZ loss. At the level of the ONL/ELM junction, hyperreflective dots were present, most noticeably in patient 13. In patient 9, parafoveal flecks were visible on NIR-AF but less visible on SW-AF.

We assessed the relationship between the central area of continuous EZ loss and signals visible in the SW-AF and NIR-AF

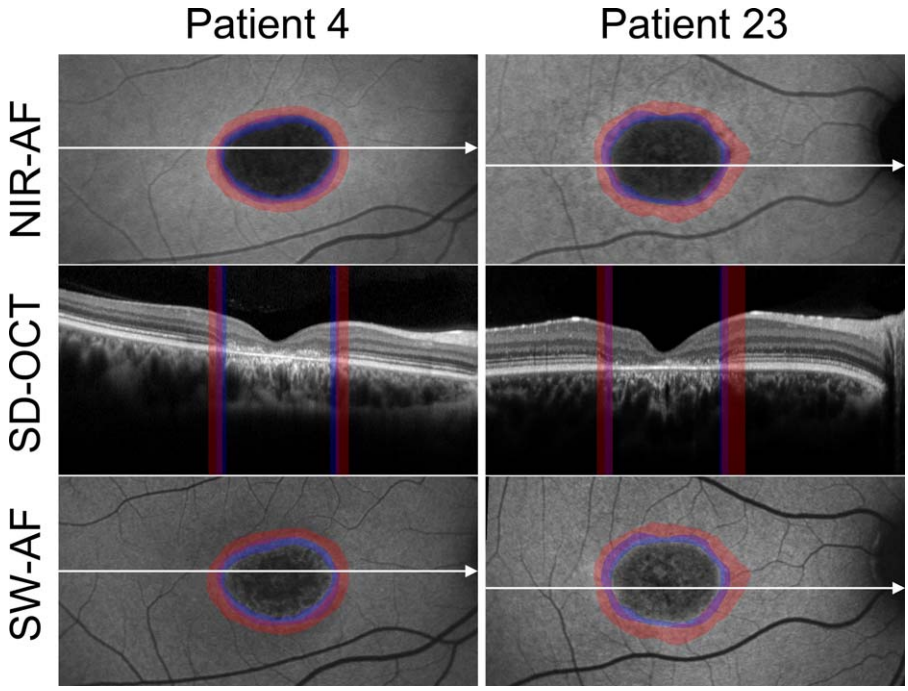

Figure 5. Spatial correspondence of high NIR-AF and SW-AF rings. Near-infrared AF, SW-AF, and SD-OCT images of patients 4 and 23. Horizontal axis and extent of SD-OCT scan indicated by *arrow* in corresponding NIR-AF and SW-AF images. The position of the high NIR-AF ring (*red*) and the high SW-AF ring (*blue*) were superimposed and indicated in each modality. Near-infrared AF, SW-AF, and SD-OCT images of patients 4 and 23 are also presented in Figure 4.

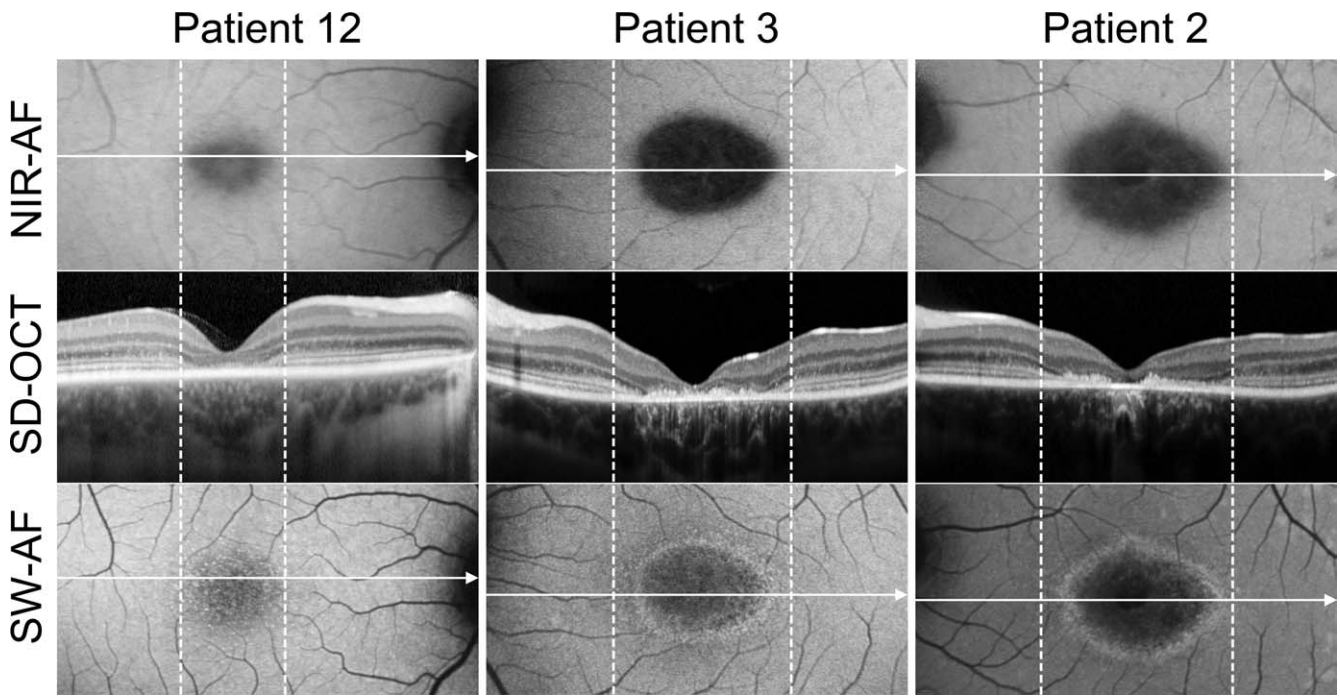

FIGURE 6. Central lesion with smooth border and no hyperautofluorescent NIR-AF ring (group 4). Near-infrared AF, SW-AF, and SD-OCT images of patients 12, 3, and 2. Horizontal axis and extent of SD-OCT scan indicated by *arrow* in corresponding NIR-AF and SW-AF images. Area of central EZ loss indicated by *dashed lines*.

images for groups 1, 3, and 4. Results are presented in Table 2. For group 1 patients, calculation of Pearson correlation coefficient revealed a strong positive correlation between the extent of EZ loss and the area of reduced NIR-AF ($r = 0.93$; $n = 10$, $P < 0.0001$); the correlation between the extent of EZ loss and the area of reduced SW-AF was more modest ($r = 0.65$; $n = 10$, $P = 0.04$). For group 3 patients, calculation of Pearson correlation coefficient revealed a strong positive correlation between the extent of EZ loss and the inner border of the NIR-AF ring ($r = 0.89$; $n = 14$, $P < 0.0001$); this correlation was stronger than the correlation between EZ loss and the inner border of the SW-AF ring ($r = 0.74$; $n = 14$, $P = 0.0027$). The

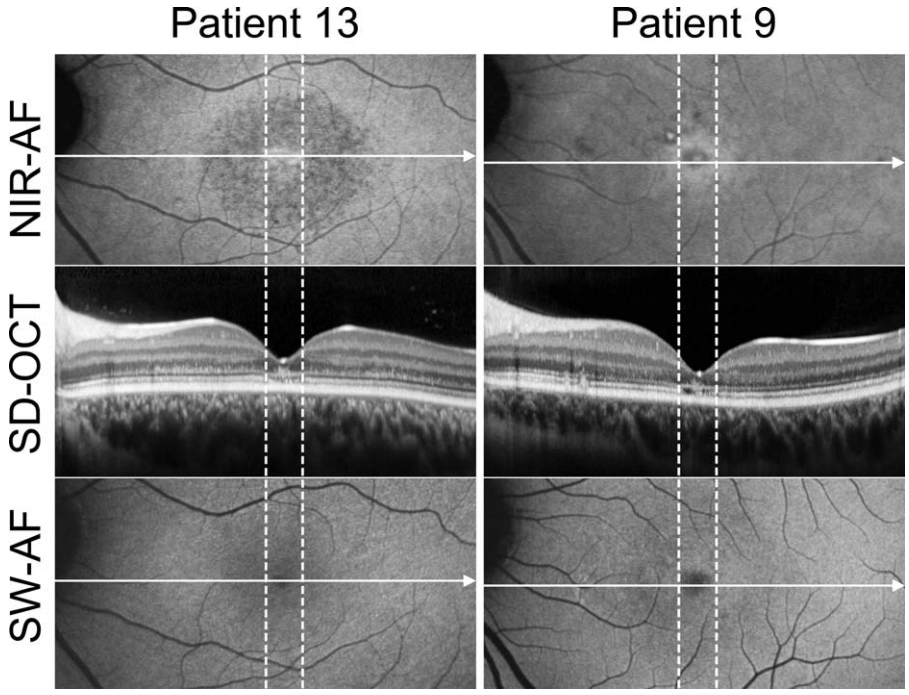

FIGURE 7. Discrete central lesions better visualized in NIR-AF images (group 5). Near-infrared AF, SW-AF, and SD-OCT images of patients 13 and 9. Horizontal axis and extent of SD-OCT scan indicated by *arrow* in corresponding NIR-AF and SW-AF images. Area of EZ disruption at fovea indicated by *dashed lines*.

Table 2. Relationship Between the Central Area of Continuous EZ Loss and Signals Visible in the SW-AF and NIR-AF Images for Groups 1, 3, and 4

Group 17 Central Lesion With Jagged Border	Extent of EZ Loss*†	Hypo-SW-AF†	Hypo-NIR-AF†
Mean length ± SEM	3.290 ± 0.1833	3.85 ± 0.17	4.11 ± 0.20
ICC	0.973	0.96	0.95
r, relative to EZ	—	0.65	0.93
P, 2-tailed	—	0.04	<0.0001
n	10	10	10
r^2	—	0.43	0.87

Group 3 Central Lesion: Smooth Border and SW- and NIR-AF Rings	Extent of EZ Loss*†	Hypo-SW-AF: Ring: Inner Diameter†	Hypo-SW-AF: Ring: Outer Diameter†	Hypo-NIR-AF: Ring: Inner Diameter†	Hypo-NIR-AF: Ring: Outer Diameter†
Mean length ± SEM	2.11 ± 0.14	1.82 ± 0.14	2.25 ± 0.16	1.89 ± 0.14	2.44 ± 0.13
ICC	1.00	1.00	0.98	0.98	0.99
r, relative to EZ	—	0.74	0.76	0.89	0.86
P, 2-tailed	—	0.0027	0.002	<0.0001	<0.0001
n	14	14	14	14	14
r^2	—	0.54	0.57	0.79	0.74

Group 4 Central Lesion: Smooth Border With No NIR-AF Ring	Extent of EZ Loss*†		SW-AF: Ring: Inner Diameter†	SW-AF: Ring: Outer Diameter†	NIR-AF: Diameter of Hypo-AF Lesion†
Mean length ± SEM	3.04 ± 0.39	2.13 ± 0.24	2.85 ± 0.13	2.50 ± 0.30	3.04 ± 0.39
ICC	1.0	1.0	0.95	0.99	1.0
r, relative to EZ	—	0.96	0.84	0.98	—
P, 2-tailed	—	0.04	0.37	0.02	—
n	4	4	4	4	4
r^2	—	0.92	0.70	0.95	—

n, number of eyes.
* Nasal to temporal outer limits of EZ loss in a horizontal plane through the fovea.
† Units of measurement are in millimeters.

coefficient of determination, r^2, in the case of the NIR-AF ring, indicated that 79% of the variance in EZ loss could be explained by variance in the position of the inner border of NIR-AF. The r^2 value describing the relationship between SW-AF ring and EZ was 0.54. In contrast to group 3 patients, analysis of the SD-OCT, NIR-AF, and SW-AF images of group 4 patients revealed that the perifoveal extent of EZ disruption was greater than the central area of reduced NIR-AF and reached eccentric positions outside the SW-AF ring diameters (inner and outer). Determination of Pearson correlation coefficient revealed a strong positive correlation between the extent of EZ loss and both the inner diameter of the SW-AF ring (r, 0.96; $n = 4$; $P = 0.04$) and the diameter of the reduced zone of NIR-AF (lesion) (r, 0.98; $n = 4$; $P = 0.02$). For all measurements that were performed in groups 1, 3, and 4, the ICC revealed excellent agreement between operators performing the quantitative analysis (Table 2).

Discussion

In the present study we compared NIR-AF and SW-AF in a cohort of genetically confirmed STGD1 patients and correlated these modalities with SD-OCT. Both the lipofuscin-associated SW-AF signal and the melanin-associated NIR-AF signal recorded at the fundus are thought to originate in RPE.[27] Choroidal melanocytes also are a source of NIR-AF; this contribution varies with iris color.[18] In STGD1 patients, SW-AF emission at the fundus is increased[4] due to augmented RPE lipofuscin. Unexpectedly, however, an overall increase in NIR-AF signal is also observed in STGD1.[16,28]

As noted in previous studies[19,29,30] and also shown here, central lesions in STGD1 often present as areas of reduced SW- and NIR-AF. Although there were similarities between SW-AF and NIR-AF patterns in our cohort, we also observed differences. For example, within the area of central EZ loss, the NIR-AF signal was typically low while the SW-AF signal was increased, decreased, or similar to surrounding areas (for example, in Fig. 2, patients 1 and 17). The zone of reduced NIR-AF was also typically larger than the area of low SW-AF (Fig. 2, patients 1 and 17; Fig. 3, patients 7 and 24; Fig. 6, patients 2 and 3). When present, flecks had a low NIR-AF signal in most cases, while the corresponding SW-AF signal was often elevated or similar to SW-AF intensities in surrounding areas (examples in Fig. 3). In addition, even when parafoveal SW-AF and NIR-AF rings overlapped, the outer border of the NIR-AF ring was generally situated at a more eccentric position (Fig. 5). Finally, in some cases we observed low NIR-AF mottling in fundus areas where the EZ was at least partially intact and the SW-AF signal appeared to be unaltered (Fig. 4, patient 14; Fig. 7, patient 13). Visual examination of the NIR-AF images along a horizontal axis through the fovea disclosed that of the 24 patients we studied, 20 presented altered NIR-AF signal at and peripheral to the central zone of EZ disruption. In groups 1 (central lesion with jagged border), 3 (central lesion with smooth border and SW- and NIR-AF rings), and 4 (central lesion with no NIR-AF ring) the extent of central EZ loss was strongly correlated with the change in NIR-AF signal.

When the EZ loss in SD-OCT images was observed only at locations where NIR-AF was reduced or absent, the implication is that RPE cell dysfunctioning and, perhaps death, occurs in advance of photoreceptor cell degeneration. Indeed, because in some patients the area of low NIR-AF exceeded the area of EZ loss (examples in Fig. 3), there can be cases in which a decline in NIR-AF can be predictive of EZ loss in SD-OCT images.

The rings of SW-AF observed in some STGD1 patients (Fig. 4) mark an annular zone wherein bisretinoid formation appeared to be increased even beyond the already elevated levels detected in the STGD1 fundus.[4,8] In keeping with our imaging protocol, photoreceptors were bleached before image acquisition in SW-AF mode; thus, it is unlikely that RPE AF unmasking due to outer segment degeneration and photopigment loss can account for the rings of increased SW-AF. On the other hand, because the central area of EZ loss often encompassed zones of hyperautofluorescent SW-AF (Fig. 2, patients 1 and 17; Fig. 3, patient 24; Fig. 4, patients 4, 14, 16, and 23; Fig. 6, patients 3 and 2), we suggest that the hyperautofluorescence of the SW-AF ring may be attributable to abnormally increased lipofuscin synthesis in disabled or degenerating photoreceptor cells. In support of this postulate, we note that RPE lipofuscin is well known to be formed in photoreceptor cells[31] and there are multiple reports indicating that in STGD1 and RP, aberrant lipofuscin-like fluorescence can be detected in human photoreceptor inner segments.[32–34] In addition, degenerating inner segments/outer segments of *Rdh8*$^{-/-}$/*Abca4*$^{-/-}$ mice emit an AF when excited by SW light.[35]

Because the NIR-AF signal is considered to be generated by melanin, the loss or diminution of NIR-AF at positions where SW-AF is present (for example, Figs. 2, 3, and 6 [patients 2 and 3]) is also puzzling. This discrepancy could reflect abnormal RPE cells with reduced or absent melanin but retention of the SW-AF signal from lipofuscin.[36] In addition, however, the possibility also exists that at least in some cases, the absence or reduction of NIR-AF may denote a loss of RPE cells. Thus, if both the NIR-AF and SW-AF signals originate from RPE, how can one account for an SW-AF signal that is present or even brighter than surrounding fundus, while NIR-AF is reduced or absent? As discussed above, one interpretation is that SW-AF can be increased in the presence of disabled and/or degenerating photoreceptor cells.

Without the benefit of NIR-AF as an additional means of tracking RPE changes in STGD1 patients, investigators were previously perplexed by the frequency with which absent SW-AF underestimated the extent of photoreceptor cell abnormalities detectable as EZ disruption in SD-OCT images.[20] Here, however, we observed that in most cases reduction in the NIR-AF signal spatially exceeded the disruption in EZ; this finding likely indicates that RPE cell loss precedes photoreceptor degeneration. In a subgroup of three patients (Fig. 6), however, the area of EZ loss extended further than the area of reduced NIR-AF. Interestingly, these patients were the youngest in our cohort and all carried the complex allele L541P/A1038V. The latter mutations are located in the exocytoplasmic domain-1 and nucleotide binding domain-1 and confer severe and relatively early-onset retina-wide disease.[37–40] In recent work using quantitative fundus AF, we also reported that the L541P/A1038V complex allele confers particularly high levels of fundus AF.[4] At positions where EZ is disrupted, the NIR-AF signal may be detectable even if the RPE cells are dysfunctional. Alternatively, this pattern could indicate that in these cases photoreceptor cells die first.

In STGD1 patients, the increase in SW-AF intensity is paralleled by a generalized increase in the NIR-AF signal.[16,28] This upturn in NIR-AF in STGD1 can be demonstrated in inferonasal fundus where a demarcation line attributable to the optic fissure becomes visible in NIR-AF images of STGD1 patients while not being detectable in the healthy eye.[28] By way of explaining the overall increase in NIR-AF signal and the NIF-AF hyperautofluorescent rings in STGD1 (Fig. 4), we have found no evidence that the bisretinoids of RPE lipofuscin can absorb and emit fluorescence in the NIR range.[25] The hyperautofluorescent rings in NIR-AF images are also unlikely to be due to a change in transmission in the retinal layers that are anterior to the RPE (unmasking), as tissue absorption at wavelengths between 600 and 1300 nm is relatively low.[41] The amount of melanin in choroidal melanocytes or in RPE cells is not known to vary so abruptly. Furthermore, pigmentary changes matching the distribution of the hyperautofluorescent NIR-AF rings are not observed in color fundus photographs (Supplementary Fig. S1). Because NIR-AF originates in melanin, one might wonder whether the increased NIR-AF intensity is generated by overlapping/superimposed RPE cells, as is observed at the borders of geographic atrophy in AMD.[42] However, thickening of the RPE/BM attributable hyperreflective layer was not visible in SD-OCT images, as can sometimes be observed with GA.[43] Nevertheless, the absence of SD-OCT changes is not confirmatory, because the optical axial depth resolution of the Spectralis SD-OCT is approximately 7 μm. Although the high AF in the junctional zone of GA often presents as foci,[44] the signal emitted at the AF rings under discussion is continuous and relatively uniform.

As an alternative, we suggest that NIR-AF may be increased if the distribution of lipofuscin-containing organelles relative to melanosomes in the RPE cell allows the lipofuscin to modulate the NIR-AF signal originating from melanin. The broadband absorbance spectrum of melanin leads to density-dependent self-absorbance of the fluorescence emitted by neighboring melanin molecules.[45] But if the packing density of melanosomes at the apex of RPE is altered in STGD1 due to the increased fractional volume of lipofuscin, quenching of the NIR fluorescence emission by secondary absorbance could be reduced. The interspersion of melanosomes with lipofuscin storage bodies, which do not absorb at NIR wavelengths, would enable more pronounced release of the fluorescence emission of melanin, with the latter being detected as enhanced NIR-AF. The organelles involved in this interaction could be melanosomes (melanin) and secondary lysosomes (lipofuscin) and/or the complex organelles described as melanolipofuscin.[46]

Limitations of the study included its relatively small number of patients. Accordingly, given the considerable clinical heterogeneity of *ABCA4*-associated disease, the large numbers of disease-associated mutations (>800), and the frequency of complex alleles (10% of patients) and compound heterozygosity,[47] we could not extract genotype-phenotype correlations from our sample of patients. Precise alignment between the AF images and the SD-OCT scan is necessary to prevent measurement error. We did not systematically monitor the alignment between simultaneously acquired NIR-R images and horizontal SD-OCT scans; horizontal alignment error with the Heidelberg Spectralis is on average 13.90 μm.[48]

In summary, we found that SW-AF changes were often not obvious at fundus locations where abnormalities were visible on NIR-AF. As noted above, within lesion areas, the low NIR-AF region was generally larger than the area of low SW-AF; in many cases the low NIR-AF signal corresponded spatially to EZ loss. This relationship is important because EZ integrity is essential for visual function.[49] This finding also underscores the clinical utility of NIR-AF imaging. The underuse of NIR-AF as compared with SW-AF may be related, in part, to the popularity of the Spectralis HRA+OCT. The OCT module in the Spectralis compromises NIR-AF signal intensity, resulting in

suboptimal NIR-AF image quality compared with confocal scanning laser ophthalmoscopy without OCT (e.g., HRA2 and Spectralis HRA), which are still commercially available but less commonly found in retinal practices. Nevertheless, NIR-AF has advantages over SW-AF. On the operational side, patients are not disturbed by the NIR-AF light; this improves patient cooperation during image acquisition, especially in young children and photophobic patients. Concerns that have been raised about long-term effects of SW light in patients with retinal disorders[16] do not apply to NIR light. Diseased versus nondiseased areas are easier to delineate in the NIR-AF images because of better contrast. Perhaps this observation is attributable to fewer gradations of signal. All of these issues favor the inclusion of NIR-AF as an outcome measure in clinical trials addressing *ABCA4*-related disease.

Acknowledgments

Supported by grants from the National Eye Institute/National Institutes of Health EY024091, EY021163, EY019007, EY019861, and EY09076; Arnold and Mabel Beckman Foundation; Foundation Fighting Blindness; and a grant from Research to Prevent Blindness to the Department of Ophthalmology, Columbia University. The authors alone are responsible for the content and writing of the paper.

Disclosure: **T. Duncker**, None; **M. Marsiglia**, None; **W. Lee**, None; **J. Zernant**, None; **S.H. Tsang**, None; **R. Allikmets**, None; **V.C. Greenstein**, None; **J.R. Sparrow**, None

References

1. Fishman GA, Farber M, Patel BS, Derlacki DJ. Visual acuity loss in patients with Stargardt's macular dystrophy. *Ophthalmology*. 1987;94:809–814.
2. Burke TR, Fishman GA, Zernant J, et al. Retinal phenotypes in patients homozygous for the G1961E mutation in the ABCA4 gene. *Invest Ophthalmol Vis Sci*. 2012;53:4458–4467.
3. Cideciyan AV, Aleman TS, Swider M, et al. Mutations in ABCA4 result in accumulation of lipofuscin before slowing of the retinoid cycle: a reappraisal of the human disease sequence. *Hum Mol Genet*. 2004;13:525–534.
4. Burke TR, Duncker T, Woods RL, et al. Quantitative fundus autofluorescence in recessive Stargardt disease. *Invest Ophthalmol Vis Sci*. 2014;55:2841–2852.
5. Cideciyan AV, Swider M, Aleman TS, et al. ABCA4-associated retinal degenerations spare structure and function of the human parapapillary retina. *Invest Ophthalmol Vis Sci*. 2005; 46:4739–4746.
6. Lois N, Halfyard AS, Bird AC, Holder GE, Fitzke FW. Fundus autofluorescence in Stargardt macular dystrophy-fundus flavimaculatus. *Am J Ophthalmol*. 2004;138:55–63.
7. Westeneng-van Haaften SC, Boon CJ, Cremers FP, Hoefsloot LH, den Hollander AI, Hoyng CB. Clinical and genetic characteristics of late-onset Stargardt's disease. *Ophthalmology*. 2012;119:1199–1210.
8. Delori FC, Staurenghi G, Arend O, Dorey CK, Goger DG, Weiter JJ. In vivo measurement of lipofuscin in Stargardt's disease—fundus flavimaculatus. *Invest Ophthalmol Vis Sci*. 1995;36:2327–2331.
9. Lopez PF, Maumenee IH, de la Cruz Z, Green WR. Autosomal-dominant fundus favimaculatus. Clinicopathologic correlation. *Ophthalmology*. 1990;97:798–809.
10. Lazow MA, Hood DC, Ramachandran R, et al. Transition zones between healthy and diseased retina in choroideremia (CHM) and Stargardt disease (STGD) as compared to retinitis pigmentosa (RP). *Invest Ophthalmol Vis Sci*. 2011;52:9581–9590.
11. Sun H, Nathans J. Stargardt's ABCR is localized to the disc membrane of retinal rod outer segments. *Nat Genet*. 1997;17: 15–16.
12. Illing M, Molday LL, Molday RS. The 220-kDa rim protein of retinal rod outer segments is a member of the ABC transporter superfamily. *J Biol Chem*. 1997;272:10303–10310.
13. Molday LL, Rabin AR, Molday RS. ABCR expression in foveal cone photoreceptors and its role in Stargardt macular dystrophy. *Nat Genet*. 2000;25:257–258.
14. Allikmets R, Singh N, Sun H, et al. A photoreceptor cell-specific ATP-binding transporter gene (ABCR) is mutated in recessive Stargardt macular dystrophy. *Nat Genet*. 1997;15: 236–246.
15. Ergun E, Hermann B, Wirtitsch M, et al. Assessment of central visual function in Stargardt's disease/fundus flavimaculatus with ultrahigh-resolution optical coherence tomography. *Invest Ophthalmol Vis Sci*. 2005;46:310–316.
16. Cideciyan AV, Swider M, Aleman TS, Roman MI, Sumaroka A, Schwartz SB. Reduced-illuminance autofluorescence imaging in ABCA4-associated retinal degenerations. *J Opt Soc Am A Opt Image Sci Vis*. 2007;24:1457–1467.
17. Delori FC, Dorey CK, Staurenghi G, Arend O, Goger DG, Weiter JJ. In vivo fluorescence of the ocular fundus exhibits retinal pigment epithelium lipofuscin characteristics. *Invest Ophthalmol Vis Sci*. 1995;36:718–729.
18. Keilhauer CN, Delori FC. Near-infrared autofluorescence imaging of the fundus: visualization of ocular melanin. *Invest Ophthalmol Vis Sci*. 2006;47:3556–3564.
19. Kellner S, Kellner U, Weber BH, Fiebig B, Weinitz S, Ruether K. Lipofuscin- and melanin-related fundus autofluorescence in patients with ABCA4-associated retinal dystrophies. *Am J Ophthalmol*. 2009;147:895–902.
20. Gomes NL, Greenstein VC, Carlson JN, et al. A comparison of fundus autofluorescence and retinal structure in patients with Stargardt disease. *Invest Ophthalmol Vis Sci*. 2009;50:3953–3959.
21. Burke TR, Tsang SH, Zernant J, Smith RT, Allikmets R. Familial discordance in Stargardt disease. *Mol Vis*. 2012;18:227–233.
22. Zernant J, Schubert C, Im KM, et al. Analysis of the *ABCA4* gene by next-generation sequencing. *Invest Ophthalmol Vis Sci*. 2011;52:8479–8487.
23. Delori FC, Greenberg JP, Woods RL, et al. Quantitative measurements of autofluorescence with the scanning laser ophthalmoscope. *Invest Ophthalmol Vis Sci*. 2011;52:9379–9390.
24. Weiter JJ, Delori FC, Wing GL, Fitch KA. Retinal pigment epithelial lipofuscin and melanin and choroidal melanin in human eyes. *Invest Ophthalmol Vis Sci*. 1986;27:145–151.
25. Duncker T, Tabacaru MR, Lee W, Tsang SH, Sparrow JR, Greenstein VC. Comparison of near-infrared and short-wavelength autofluorescence in retinitis pigmentosa. *Invest Ophthalmol Vis Sci*. 2013;54:585–591.
26. Staurenghi G, Sadda S, Chakravarthy U, Spaide RF. Proposed lexicon for atomic landmarks in normal posterior segment spectral-domain optical coherence tomography: the IN*OCT consensus. *Ophthalmology*. 2014;121:1572–1578.
27. Gibbs D, Cideciyan AV, Jacobson SG, Williams DS. Retinal pigment epithelium defects in humans and mice with mutations in MYO7A: imaging melanosome-specific autofluorescence. *Invest Ophthalmol Vis Sci*. 2009;50:4386–4393.
28. Duncker T, Lee W, Tsang SH, et al. Distinct characteristics of inferonasal fundus autofluorescence patterns in Stargardt disease and retinitis pigmentosa. *Invest Ophthalmol Vis Sci*. 2013;54:6820–6826.
29. Cukras CA, Wong WT, Caruso R, Cunningham D, Zein W, Sieving PA. Centrifugal expansion of fundus autofluorescence

patterns in Stargardt disease over time. *Arch Ophthalmol*. 2012;130:171–179.

30. Schmitz-Valckenberg S, Lara D, Nizari S, et al. Localisation and significance of in vivo near-infrared autofluorescent signal in retinal imaging. *Br J Ophthalmol*. 2011;95:1134–1139.
31. Sparrow JR, Wu Y, Kim CY, Zhou J. Phospholipid meets all-*trans*-retinal: the making of RPE bisretinoids. *J Lipid Res*. 2010;51:247–261.
32. Szamier RB, Berson EL. Retinal ultrastructure in advanced retinitis pigmentosa. *Invest Ophthalmol Vis Sci*. 1977;16:947–962.
33. Bunt-Milam AH, Kalina RE, Pagon RA. Clinical-ultrastructural study of a retinal dystrophy. *Invest Ophthalmol Vis Sci*. 1983; 24:458–469.
34. Birnbach CD, Jarvelainen M, Possin DE, Milam AH. Histopathology and immunocytochemistry of the neurosensory retina in fundus flavimaculatus. *Ophthalmology*. 1994;101:1211–1219.
35. Flynn E, Ueda K, Auran E, Sullivan JM, Sparrow JR. Fundus autofluorescence and photoreceptor cell rosettes in mouse models. *Invest Ophthalmol Vis Sci*. 2014;55:5643–5652.
36. Eagle RC, Lucier AC, Bernardino VB, Yanoff M. Retinal pigment epithelial abnormalities in fundus flavimaculatus. *Ophthalmol*. 1980;87:1189–1200.
37. Rivera A, White K, Stöhr H, et al. A comprehensive survey of sequence variation in the ABCA4 (ABCR) gene in Stargardt disease and age-related macular degeneration. *Am J Hum Genet*. 2000;67:800–813.
38. Lewis RA, Shroyer NF, Singh N, et al. Genotype/phenotype analysis of a photoreceptor-specific ATP-binding cassette transporter gene, ABCR, in Stargardt disease. *Am J Hum Genet*. 1999;64:422–434.
39. Cideciyan AV, Swider M, Aleman TS, et al. ABCA4 disease progression and a proposed strategy for gene therapy. *Hum Mol Genet*. 2009;18:931–941.
40. Wiszniewski W, Zaremba CM, Yatsenko AN, et al. ABCA4 mutations causing mislocalization are found frequently in patients with severe retinal dystrophies. *Hum Mol Genet*. 2005;14:2769–2778.
41. Tsai CL, Chen JC, Wang WJ. Near-infrared absorption property of biological soft tissue constituents. *J Med Biol Engineering*. 2001;21:7–14.
42. Rudolf M, Vogt SD, Curcio CA, et al. Histologic basis of variations in retinal pigment epithelium autofluorescence in eyes with geographic atrophy. *Ophthalmology*. 2013;120:821–828.
43. Fleckenstein M, Issa PC, Helb HM, et al. High-resolution spectral domain-OCT imaging in geographic atrophy associated with age-related macular degeneration. *Invest Ophthalmol Vis Sci*. 2008;49:4137–4144.
44. Holz FG, Bellmann C, Margaritidis M, Schutt F, Otto TP, Volcker HE. Patterns of increased in vivo fundus autofluorescence in the junctional zone of geographic atrophy of the retinal pigment epithelium associated with age-related macular degeneration. *Graefes Arch Clin Exp Ophthalmol*. 1999;237: 145–152.
45. Riesz J, Gilmore J, Meredith P. Quantitative scattering of melanin solutions. *Biophys J*. 2006;90:4137–4144.
46. Feeney L. Lipofuscin and melanin of human retinal pigment epithelium. Fluorescence, enzyme cytochemical and ultrastructural studies. *Invest Ophthalmol Vis Sci*. 1978;17:583–600.
47. Shroyer NF, Lewis RA, Yatsenko AN, Wensel TG, Lupski JR. Cosegregation and functional analysis of mutant *ABCR* (*ABCA4*) alleles in families that manifest both Stargardt disease and age-related macular degeneration. *Hum Mol Genet*. 2001; 10:2671–2678.
48. Barteselli G, Bartsch DU, Viola F, et al. Accuracy of the Heidelberg Spectralis in the alignment between near-infrared image and tomographic scan in a model eye: a multicenter study. *Am J Ophthalmol*. 2013;156:588–592.
49. Wong IY, Iu LP, Koizumi H, Lai WW. The inner segment/outer segment junction: what have we learnt so far? *Curr Opin Ophthalmol*. 2012;23:210–218.

Investigative Ophthalmology & Visual Science